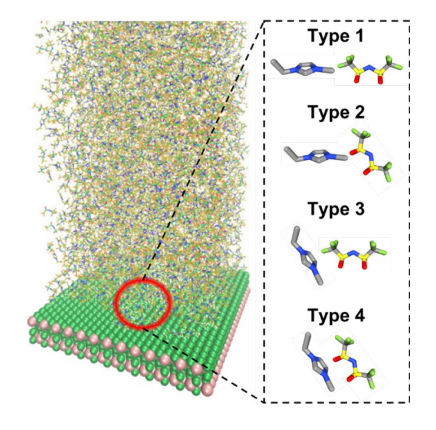
Innermost Ion Association Configuration is a Key Structural Descriptor of Ionic Liquids at Electrified Interfaces

Kaustubh S. Panse^{1,2}†, Haiyi Wu^{3,4}†, Shan Zhou^{1,2}, Fujia Zhao^{1,2}, Narayana R. Aluru^{3,4}* and Yingjie Zhang^{1,2}*

- 1. Department of Materials Science and Engineering, University of Illinois, Urbana, IL 61801, USA
- 2. Materials Research Laboratory, University of Illinois, Urbana, IL 61801, USA
- 3. Walker Department of Mechanical Engineering, The University of Texas at Austin, Austin, TX 78712, USA
- 4. Oden Institute for Computational Engineering & Sciences, The University of Texas at Austin, Austin, TX 78712, USA
- †These authors contributed equally to this work
- *Correspondence to: yjz@illinois.edu (Y.Z.) or aluru@utexas.edu (N.R.A.)

ABSTRACT: The structure of electric double layers (EDLs) is crucial for all types of electrochemical processes. While in dilute solutions EDL structure can be approximately treated within the Gouy-Chapman-Stern regime, in highly ionic electrolytes the description of EDL has been largely elusive. Here we study the EDL structure of an ionic liquid on a series of crystalline electrodes. Through molecular dynamics (MD) simulations, we observe strong intermolecular interaction among cations and anions, and propose that the cation-anion association structure at the innermost layer is a key descriptor of the EDL. Using our recently developed electrochemical 3D atomic force microscopy (EC-3D-AFM) technique, we confirm the theoretical prediction, and further find that the width of the first EDL is an experimental gauge of the ion association structure in that layer. We expect such ion association descriptors to be broadly applicable to a large range of highly ionic electrolytes on various electrode surfaces.

TOC Graphic



Liquid-solid interfaces are critical for the functions of a large range of natural and engineered processes, ranging from biological signal transduction to water filtration and electrochemical energy conversion.¹⁻⁴ At these interfaces, EDLs form ubiquitously due to a combination of multiple interaction effects such as surface adsorption, electrostatic interaction, van der Waals force, and hydrogen bonding. As a result of the convoluted intermolecular and molecule-electrode interactions, the structure of EDLs remains elusive. In order to understand and design the EDLs, tremendous efforts have been devoted to finding their structural descriptors. As an example, in the most widely studied electrolyte, aqueous solutions with low or intermediate salt concentration (\le \text{...} ~1 M), Gouy-Chapman-Stern model predicts the co-existence of two regions with distinct properties: a discrete Stern layer and a diffuse layer.⁵ The Stern layer is typically assumed to be occupied mainly by water, where the hydrogen bond configuration is oftentimes used as a key descriptor; ⁶⁻⁸ in contrast, for the diffuse layer, Debye length is the crucial descriptor characterizing the width of the charged regions that screen the electrode potential.^{9,10} In various electrochemical processes, either descriptor may play a critical role. For example, in water splitting reactions, Stern layer hydrogen bond configurations have been observed to have a large impact on the catalytic activity; 11,12 in capacitive charging processes, in contrast, Debye length has been regarded as the key factor determining the charge density. 9,13,14

In recent years, highly ionic electrolytes, such as ionic liquids and highly concentrated (a few molar) aqueous/organic solutions, have gained strong interest for various electrochemical applications including batteries, supercapacitors, and electrolyzers. ^{15–20} Due to the strong Coulomb interaction among the charged species, the EDL structure of these electrolytes is found to strongly deviate from the Gouy-Chapman-Stern model. ^{21,22,31,32,23–30} In particular, both MD simulation and AFM imaging have revealed multiple discrete molecular layers in the EDL of various ionic liquids and concentrated aqueous solutions. ^{21–29,32} However, despite the knowledge on the spatial density distributions, a quantitative understanding of the structural factors controlling the EDL configuration and capacitive charging behaviors is still lacking. As a result, we are still not able to rationally design molecular structures to achieve favorable EDLs for targeted applications.

In this work, we perform MD simulation and EC-3D-AFM imaging to examine the structural descriptor of the EDL of 1-ethyl-3-methylimidazoliumbis(trifluoromethylsulfonyl)imide (EMIMTFSI), a widely studied ionic liquid system that has a large electrochemical stability window and low volatility. We investigate the EDL on a series of crystalline electrodes including MoS₂ flakes and highly oriented pyrolytic graphite (HOPG), the former electrocatalytically active in ionic liquids while the latter serving as a model system for supercapacitor and battery electrodes. Hoth types of electrodes allow the preparation of atomically clean surfaces immersed in the ionic liquid electrolyte, which further enable a reliable comparison between simulation and experimental data. We observe that the first EDL of EMIM-TFSI mainly consists of associated complexes of EMIM+ cations and TFSI- anions, and that the EMIM+-TFSI- association configuration (orientation and separation) in this innermost EDL is a key descriptor of the overall EDL capacitive charging effect.

We have previously studied the EMIM-TFSI/HOPG system, and identified the molecular density and orientation distribution at a range of electrode potentials. Onsidering that the EDL structure should depend on both the intermolecular force among species in the electrolyte and the electrode-electrolyte interaction, it is desirable to study other electrodes beyond HOPG, in order to separate the contribution from different factors and decipher the universal structural descriptors of the EDL. Comparing HOPG with MoS₂, the former has been reported to show strong van der Waals / π – π

interaction with the carbon-rich cations in most ionic liquids, $^{42-44}$ while the latter does not have such interactions. Therefore, here we investigate MoS₂ electrodes and compare the results with those from the HOPG system.

We first construct an MoS₂/EMIM-TFSI/MoS₂ sandwich system for MD simulation, with detailed methods, overall snapshot and convergence/equilibration verification shown in the Supporting Information ("Methods" section and Figures S1 and S2). Same as that of the HOPG/EMIM-TFSI/HOPG system (Figure S3), the two MoS₂ electrodes are placed 16 nm apart (Figure S1), which ensures that the EMIM-TFSI at the center of the channel exhibits bulk liquid behavior. ⁴⁵ At the potential of zero charge (PZC), all the sulfur and molybdenum atoms are assigned the intrinsic partial charges of -0.3 e and 0.6 e, respectively. To investigate the impact of the electrode's charge doping / potential, we apply additional charges uniformly to all the atoms in the MoS₂ layers that are in direct contact with the ionic liquid. The excess charges in the two opposite electrodes have the same density but reverse sign, to ensure charge neutrality in the overall MD system. We set up MD simulations with five different surface charge densities: $\sigma_s = 0, \pm 0.24 \text{ e/nm}^2, \pm 0.45 \text{ e/nm}^2$. The corresponding electrode potentials are calculated after the MD production run, by solving Poisson's equation using the equilibrium charge density distribution in the electrolyte. The details of the calculated charge density and potential profiles in the electrolyte can be found in Figure S4. The electrode potentials corresponding to the five different charge densities are found to be PZC, PZC + 0.90 V, PZC - 0.72 V, PZC + 1.43 V, and PZC - 1.48 V, respectively.

From the simulated MD trajectories, we extract and plot the center-of-mass (COM) density distribution of EMIM⁺ and TFSI⁻ along the z direction (Figure 1a). As the electrode potential changes, we observe pronounced COM reconfiguration mainly within ~0.67 nm from the electrode surface. At z > 0.67 nm, the COM densities show quasi-periodic variations as a function of z, but the overall profiles are largely independent of the electrode potential except some small z offsets. Within 0 - 0.67 nm, the region highlighted in Figure 1a, we observe much higher COM densities, and both the peak position and intensity change significantly at different electrode potentials. The peak position shifts result from electrostatic interactions with the electrode. That is, beginning from a largely overlapping profile at PZC, cations move away from, while anions move towards the electrode surface at more positive electrode potentials; at negative potentials, the reverse trend is observed. In the whole potential range, the cations and anions co-exist in this 0 - 0.67 nm region, indicating that strong intermolecular interactions are likely responsible for holding the ions together. Therefore, we treat this region as a whole, and label it as the first EDL, rather than separating it into two or more layers with convoluted and oftentimes overlapping positions.

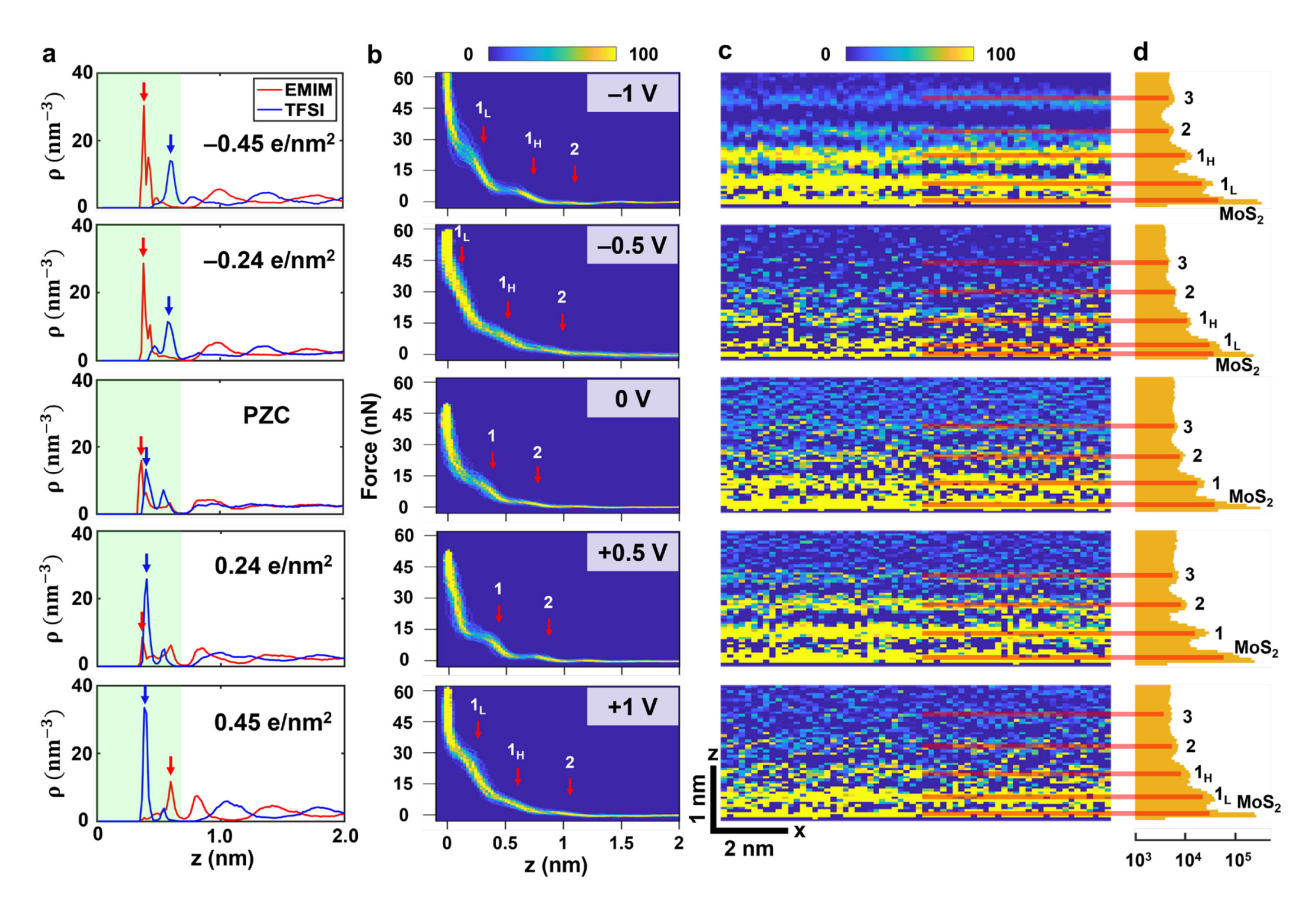


Figure 1. Combined simulation and experimental quantification of the EDL molecular density of MoS₂/EMIM-TFSI. (a) MD simulated COM profiles of EMIM⁺ and TFSI⁻ along the z direction at different electrode charge densities, where the first EDL (0<z<0.67 nm) is shaded in green with arrows marking the peak positions. (b) EC-3D-AFM measured force *vs* z bivariate histograms at a series of electrode potentials, where EDL layer positions are marked by red arrows. (c) and (d) are the x-z count maps and count histograms as a function of z, respectively, corresponding to the same EC-3D-AFM data shown in (b). The red lines connecting (c) and (d) show the positions of the electrode surface and EDL (sub-)layers.

To quantify the contribution of the first EDL layer to the overall EDL charge storage function, we integrate the charge density over z in the 0-0.67 nm region, and compare with the electrode charge density. As shown in Figure S5, the first EDL is capable of screening most of the electrode charge. Therefore, this small region plays a dominant role in EDL capacitive charging. Within the first EDL, we further find strongly anisotropic, potential-dependent molecular orientation (Figure S6b). In general, molecules that are attracted to the electrode surface (by the counter charges at the electrode) tend to have in-plane orientation, while the ones repelled away from the electrode are mostly tilted or vertical. In contrast, in the upper EDL layers, the molecular orientation is nearly isotropic (Figure S6c, d), similar to that of the bulk liquid (Figure S7). For the rest of the MD simulations in this work, we focus on the first EDL layer.

Despite the differences in the electrode structure, we find that the simulated EDL structure of EMIM-TFSI on MoS₂ and HOPG are surprisingly similar (Figures 1a, S6, and S8). This reveals

that the possible electrode-specific interactions (e.g., π – π interaction, specific adsorption, or other van der Waals interactions between the electrode and electrolyte) are much weaker than the effects of the interfacial electric field and intermolecular interactions among the ionic species. We expect that such weak electrode-dependence may be relevant for EDLs of a large range of highly ionic electrolytes where intermolecular Coulomb interaction is strong.

To verify that the MD simulation results closely resemble the realistic systems, we perform EC-3D-AFM of EMIM-TFSI on an MoS₂ flake to reveal the EDL structure (see Supporting Information for detailed methods). The obtained force curves and molecular density distribution, shown in Figure 1b–d, again closely mimic those of HOPG/EMIM-TFSI.⁴¹ In particular, we find that the most pronounced EDL reconfiguration at different potentials occurs within the first EDL, which consists of either one or two force spikes. When the electrode potential is sufficiently high, we observe the splitting of this layer into two sub-layers, same as those in the MD simulation results (Figure 1a). Direct comparison between the peak positions in the first EDL of the MD and EC-3D-AFM results reveal that the overall trend is consistent (Figure S9), while the small differences in the exact peak position values are likely due to the finite molecular size and the real-time repulsion between the AFM tip and the molecules in the EDL (Figure S10).

Considering that the molecules are dynamically moving and rotating in the EDL, the timeaveraged density and orientation profiles of individual species shown in Figures 1a and S6, although important, are insufficient to describe the full molecular structure of EDL. A key missing piece of information is the dynamic interaction and coordination of each species with its neighboring molecules. In bulk liquids, the intermolecular coordination structure is usually quantified by the radial distribution function (RDF), which is a key descriptor of the liquid's molecular configuration. Here we adopt this approach to further elucidate the EDL structure. We compute the in-plane RDF of all the possible pairs of species in the ionic liquid, including EMIM⁺-EMIM⁺, TFSI⁻-TFSI⁻, and EMIM⁺-TFSI⁻, in the first EDL of EMIM-TFSI/MoS₂. For EMIM⁺-TFSI, we calculate both the RDF of EMIM surrounding a TFSI ion, and that of TFSI surrounding EMIM⁺. As shown in Figure 2a, the RDFs of all the ion pairs exhibit multiple peaks at all the electrode potentials, due to the intermolecular interaction effects. More negative potentials tend to favor smaller EMIM⁺-EMIM⁺ distance (first RDF peak) due to the accumulation of cations in the first EDL, and similarly more positive potentials lead to smaller TFSI-TFSI distance. However, note that the potential-dependence of the first RDF peak of TFSI-TFSI is weaker than that of EMIM⁺-EMIM⁺, likely because of the nearly perfectly flat orientation of TFSI⁻ at positive potentials (Figure S6b) that limits the intermolecular distance, counter-balancing the increase in molecular density. The RDFs for EMIM⁺ near TFSI⁻ and TFSI⁻ near EMIM⁺ are mostly the same at the same electrode potentials, as expected for the well-mixed fluid state. At all the electrode potentials studied, the first EMIM⁺-TFSI⁻ RDF peak always occurs at ~0.5 nm, and its first prominent local minimum occurs at ~0.95 nm. These distances are always smaller than those of EMIM⁺-EMIM⁺ and TFSI⁻-TFSI⁻ at any potential. The close distance and its potentialindependence (along the in-plane directions) reveal a strong intermolecular interaction between cations and anions, in contrast to the much weaker EMIM⁺-EMIM⁺ and TFSI⁻-TFSI⁻ interactions. Therefore, the EMIM⁺-TFSI⁻ coordination is the most critical factor describing the intermolecular configuration within the first EDL.

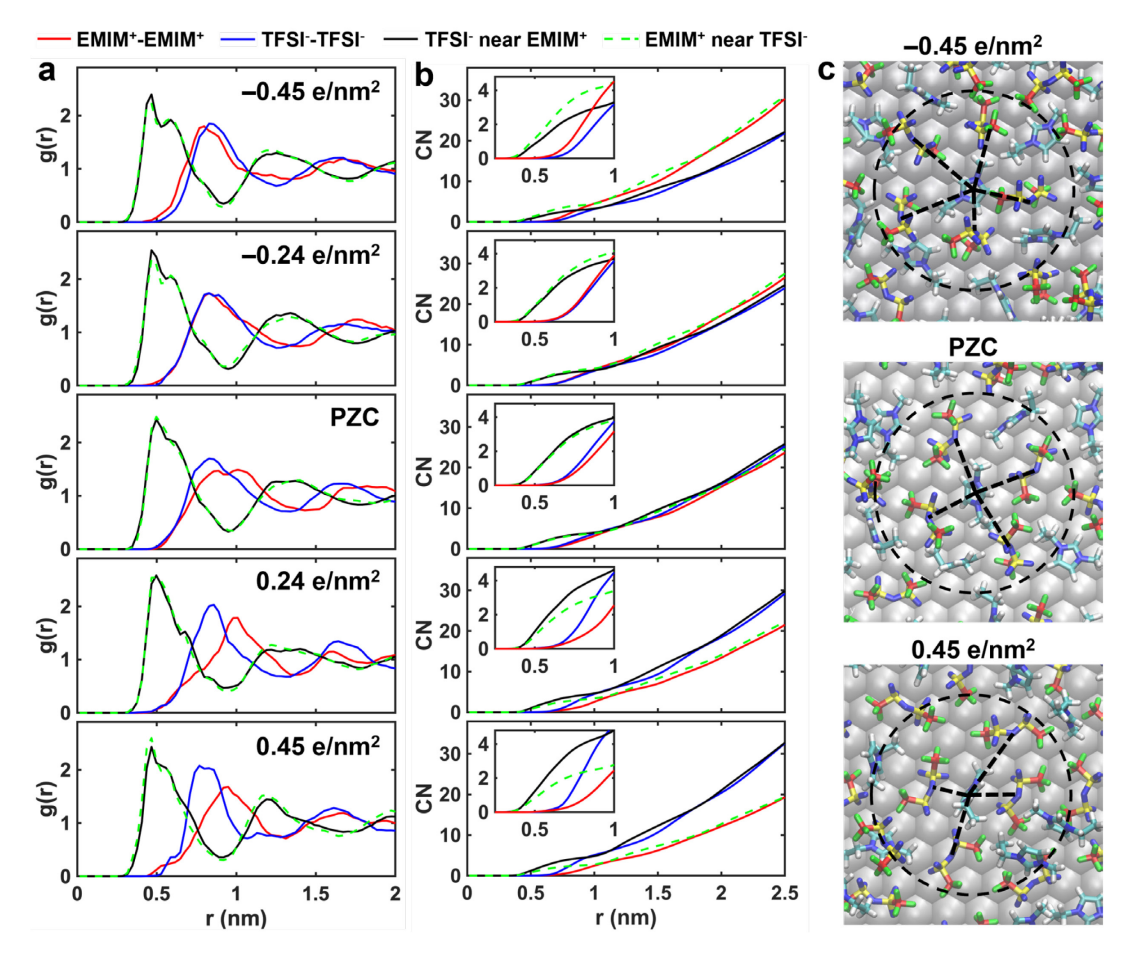


Figure 2. MD simulation of the intermolecular coordination structures in the first EDL of EMIM-TFSI on MoS₂. (a) In-plane RDF profiles calculated for EMIM⁺-EMIM⁺, TFSI⁻-TFSI⁻, and EMIM⁺-TFSI⁻ (EMIM⁺ surrounding TFSI⁻ or TFSI⁻ surrounding EMIM⁺) at different electrode potentials. (b) Coordination number profiles. (c) Snapshots showing intermolecular coordination structures of TFSI⁻ surrounding EMIM⁺, where the circle has a radius of 0.95 nm corresponding to the first pronounced local minimum in the RDF of EMIM⁺-TFSI⁻, and the dashed lines connect TFSI⁻ molecules to the central EMIM⁺.

We further calculate the coordination number (CN) of ion pairs based on the in-plane RDF profiles via $CN_{AB} = \rho_B \int_0^r g_{AB}(r) 2\pi r dr$, where CN_{AB} is the CN of B molecules surrounding an A molecule, ρ_B is the average areal density of molecule B, g_{AB} is the RDF of B surrounding A, and r is the distance between A and B. The CNs for all types of ion pairs are shown in Figure 2b. We observe that the CNs are dominated by the average surface density at $r > \sim 2.0$ nm at all the potentials. Specifically, in this long-distance range, CNs of TFSI⁻-TFSI⁻ and TFSI⁻ near EMIM⁺ largely overlap with each other, both governed by the average density of TFSI⁻; similarly, CNs of EMIM⁺-EMIM⁺ and EMIM⁺ near TFSI⁻ also mostly overlap as determined by the average EMIM⁺ density. At potentials away from PZC, clear offsets between these two sets of curves at $r > \sim 2.0$ nm are observed, due to the potential-modulated differences of the cation vs anion density as shown in Figures 1a and S5.

In the small distance range (0.25 nm < r < 1.0 nm, insets in Figure 2b), the behavior of CN is drastically different. While the overall intensities are still affected by the potential-modulated molecular density of each species, the EMIM⁺-TFSI⁻ CNs start to increase at a much smaller r compared to those of EMIM⁺-EMIM⁺ and TFSI⁻-TFSI⁻, as consistent with the RDF results in Figure 2a. At the end of the first RDF peak, r~0.95 nm, the CN of EMIM⁺-TFSI⁻ lies in the range of 2 to 5, revealing that each ion coordinates with multiple counter-ions. To examine the EMIM⁺-TFSI⁻ coordination structure, we take snapshots of the molecules in the first EDL at different potentials, as shown in Figure 2c. We observe multiple TFSI⁻ molecules surrounding one EMIM⁺ within a distance of r \leq 0.95 nm, in agreement with the RDF and CN results. The snapshots also reveal varying EMIM⁺-TFSI⁻ coordination configurations at each potential and between different potentials. However, due to the dynamic nature of these molecules and intermolecular interactions, the series of individual snapshots are insufficient to provide statistically significant ion association structures.

To better quantify the EMIM⁺-TFSI⁻ association configuration and its potential dependence, we sort the pairing structure into four categories with different molecular orientation (Figure 3a). Type 1: both EMIM⁺ and TFSI⁻ are close to the parallel direction (relative to the electrode surface), with angles (defined in Figure S6a) of $\theta_E \in (0^\circ\text{-}50^\circ\text{ or }130^\circ\text{-}180^\circ)$ and $\theta_T \in (60^\circ\text{-}120^\circ)$, respectively; type 2: EMIM⁺ is near the parallel direction with $\theta_E \in (0^\circ\text{-}50^\circ\text{ or }130^\circ\text{-}180^\circ)$, while TFSI⁻ is nearly parallel to the surface with $\theta_T \in (60^\circ\text{-}120^\circ)$; type 4: both EMIM⁺ and TFSI⁻ are tilted with $\theta_E \in (50^\circ\text{-}130^\circ)$ and $\theta_T \in (0^\circ\text{-}60^\circ\text{ or }120^\circ\text{-}180^\circ)$, respectively. Note that only the EMIM⁺ and TFSI⁻ molecules with $r \le 0.95$ nm are considered as associated complexes and are taken into account in any of the four categories. The probability distribution of the four types of pairing structures is shown in Figure 3b. At PZC, all four types have similar probability. At positive potentials, type 3 becomes dominant, followed by type 1, as a result of the flattening of the TFSI-molecules and the tilting of EMIM⁺. At negative potentials, type 2 and type 4 ion pairs are favored, due to the tilting of TFSI⁻. These trends are consistent with the angular distribution results of individual ions shown in Figure S6b.

Note that an EMIM⁺-TFSI⁻ association complex can consist of more than two molecules, as shown in Figure 2b, c. Nevertheless, since each multi-ion complex is still composed of multiple ion pairs (some of which may share a common cation/anion), the distribution of the individual EMIM⁺-TFSI⁻ pair configurations still represents the overall structure of all the EMIM⁺-TFSI⁻ complexes in the first EDL. Therefore, the innermost ion pair configuration is a good structural descriptor of the EDL.

In addition to the molecular orientation, the vertical separation between EMIM⁺ and TFSI⁻ in ion pairs is also an important structural factor. Figure 3c shows the average z offset between the COM of EMIM⁺ and TFSI⁻ in their ion pairs at different potentials. We observe that, consistent with Figure 1a, the vertical distance between molecules in ion pairs also follows electrostatic modulations. That is, anions move towards the electrode while cations move farther away at more positive potentials, leading to more positive cation-anion z offset; and the reverse trend occurs for negative potentials.

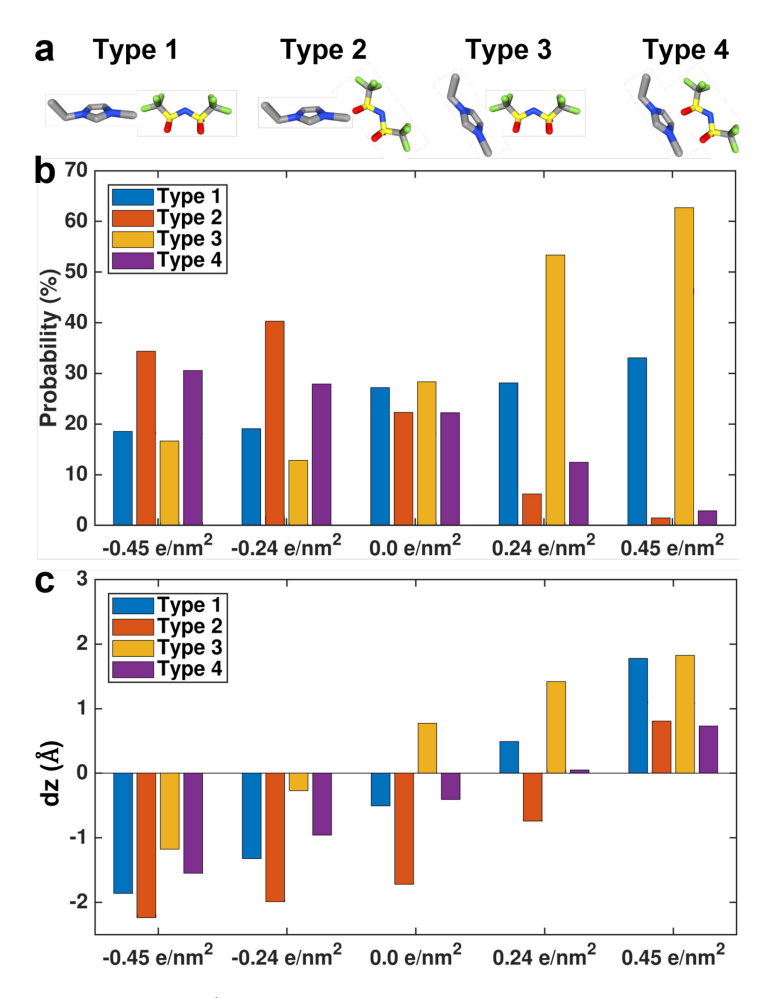


Figure 3. Classification of EMIM⁺-TFSI⁻ pairing structures and their potential dependence (on MoS₂ electrode). (a) Schematics of four types of EMIM⁺-TFSI⁻ ion pair configurations. (b) Probability distribution of the four types of ion pairs at a series of electrode potentials. (c) z-offset between EMIM⁺ and TFSI⁻ in each type of ion pairs as a function of the electrode potential.

Since the EMIM⁺-TFSI⁻ pairing configuration within the first EDL represents both the dynamic intermolecular interaction effects and the electrostatic modulation from the charged electrode, it enables a thorough description of the EDL structure and capacitive charging effects. In addition, we perform further MD simulation of EMIM-TFSI on HOPG, and observe similar ion association effects (Figures S11 and S12). Therefore, we expect the innermost ion association configuration to be a key descriptor of the EDL structure for a large range of ionic liquid / electrode interfaces.

Note that intermolecular interaction effects in ionic liquids have been previously studied by Kornyshev *et al.* in a continuum theory,³⁰ where they predicted that short-range Coulomb correlation results in "overscreening" in the EDL at small electrode potentials. Our ion association descriptor of EMIM-TFSI agrees with this prediction, and provides a molecular basis for the Kornyshev overscreening theory. In fact, the ion association configurations shown in Figures 2 and 3 can be viewed as molecular representations of the intermolecular correlation effects assumed by Kornyshev *et al.* Due to the strong ion association effects, we indeed observe overscreening, where the areal charge density of the first sub-layer in the EDL is larger than that of the electrode

(Figure S5b). On the other hand, Kornyshev *et al.* also predicted "crowding" effect at high electrode potentials, which we do not observe in our results. This is likely due to three possible factors: 1) the range of electrode potential we study is not high enough to induce crowding; 2) the ion association strength in our EMIM-TFSI system is much higher than the phenomenological correlation term assumed by the Kornyshev model; 3) the EMIM⁺ and TFSI⁻ molecules (see Figure 3a) strongly deviate from the spherical shape assumed in the Kornyshev model, and the orientational reconfiguration, in addition to the COM rearrangement of the molecules, effectively screen the electrode potential (Figures 3 and S6) and prevent crowding effect from occurring.

Now that we have predicted the ion association descriptor through MD simulations, it is desirable to find an experimental observable that represents this descriptor. However, this is a nontrivial task, as experimental results oftentimes contain less information on the dynamically interacting molecular structure. In the case of EC-3D-AFM, while the characteristic EDL imaging results shown in Figure 1b–d reveal the overall molecular density distribution, it is still not clear which parameter represents the ion association effect in the EDL.

To experimentally quantify the ion association effect in the first EDL, we extend the EDL imaging to multiple electrode-electrolyte interface regions (EMIM-TFSI on a series of MoS₂ flakes and HOPG electrodes), and use two different EC-3D-AFM imaging modes (DC and AC), in order to extract the common, characteristic features. Due to the semiconducting nature and presence of significant amounts of sulfur vacancies, mechanically exfoliated MoS₂ is expected to have large variations in the local doping level and surface potential. HOPG is a semimetal and is observed to have uniform surface potential (after fresh exfoliation). This makes HOPG an ideal system to apply different imaging modes and observe the universal EDL features.

Considering that the count vs z histograms clearly resolve the positions of the EDL layers on flat electrodes (Figure 1d), we process and plot these histograms for a total of five local electrode regions, including three MoS₂ flakes and two different HOPG areas, as shown in Figure 4a-e. In addition, we perform AC mode EC-3D-AFM on another HOPG area and use phase to represent the EDL structure (Figure 4f).⁴¹ At each region, we first image the surface structure of the electrode at each potential before taking EC-3D-AFM measurements, and only the regions that are atomically clean throughout the whole potential range are considered here. This strict criterion enables the reliable observation of the intrinsic potential-dependent EDL structure. At the same time, it sets limits for the potential range we can apply at each region, since solid clusters tend to form on the electrode surface stochastically at non-zero potentials (likely due to parasitic redox processes of impurities).⁴¹ Despite these constraints, we are able to obtain clean EC-3D-AFM maps at a series of at least four different electrode potentials for each of the six regions shown in Figure 4. At different MoS₂ flakes, we observe similar potential-dependent multi-layered EDL structures (Figure 4a-c). At a potential between 0 - 0.5 V vs Pt, the z position for each EDL layer reaches a minimum value; as the potential moves away from this point, in either the positive or negative direction, the EDL z positions increase. Based on our MD simulation results, we assign the potential corresponding to the smallest z position (for each layer) as the PZC. Therefore, the PZC estimated from the z histograms is different for each of the three MoS₂ flakes, with values varying in the range of 0 - 0.5 V (vs Pt). This is likely due to the surface potential variations of the MoS₂ surface as a result of the random distribution of sulfur vacancies and the induced doping fluctuations. In contrast to the PZC variations observed on MoS₂, we find nearly the same EDL structures with PZC near 0 V on different areas of HOPG, regardless of the EC-3D-AFM imaging mode. All of the HOPG EDL results (Figure 4d–f) resemble those of the first MoS₂ flake (Figure 4a), where the z position of each layer increases gradually as the potential deviates from 0 V.

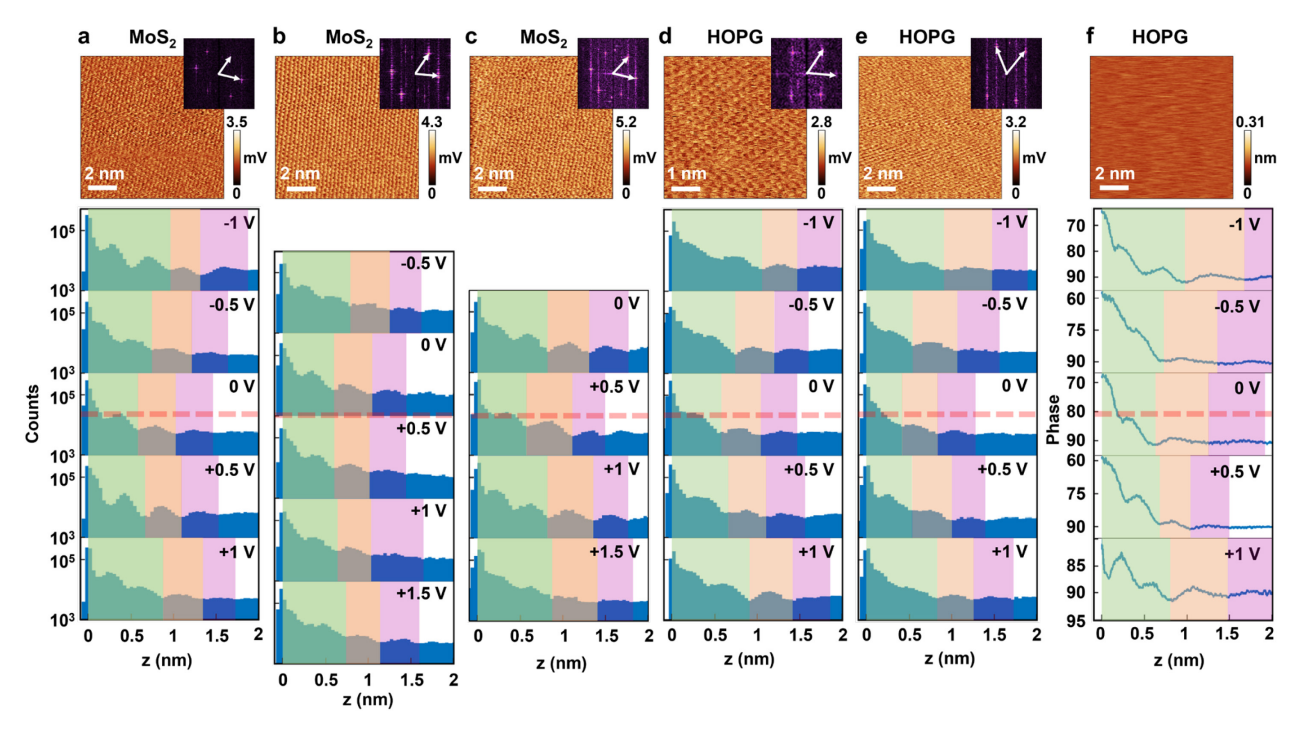


Figure 4. Experimental quantification of the EDL structure of EMIM-TFSI on a series of electrodes. ($\mathbf{a} - \mathbf{c}$) Count histograms vs z on three MoS₂ flakes. (\mathbf{d} , \mathbf{e}) Count histogram vs z at two HOPG areas. ($\mathbf{a} - \mathbf{e}$) are all obtained from DC mode EC-3D-AFM. (\mathbf{f}) Average phase vs z curves for another HOPG area (different from the areas in d and e) extracted from AC mode EC-3D-AFM. In all of the results, the 1st, 2nd and 3rd EDL layers are highlighted in green, orange and purple, respectively. The horizontal red dashed lines cross the frames where the 1st EDL width is minimum. The top panel of each column shows the x-y lateral ($\mathbf{a} - \mathbf{e}$) or height (\mathbf{f}) image of the corresponding electrode surface, with the Fourier transform shown as insets in ($\mathbf{a} - \mathbf{e}$) (11 nm⁻¹ × 11 nm⁻¹ each). All the areas are found to be atomically clean, although lattices cannot be resolved in (\mathbf{f}) due to the strong damping of cantilever oscillation (required in the AC mode) in the highly viscous ionic liquid.

In addition, we perform AC mode force curve measurements of EMIM-TFSI on a silicon surface, and observe similar results as EMIM-TFSI/HOPG (Figure S13), further confirming the generality of the ion association effect.

The local doping variations of MoS₂ flakes are further supported by our confocal Raman mapping (Figures S14 and S15) and Kelvin probe force microscopy (KPFM) (Figure S16) results. In fact, the surface potential variations observed in KPFM is a few hundred mV, in the same scale as the PZC fluctuations we find in EC-3D-AFM results. Note that, although the mechanically exfoliated MoS₂ flakes likely contain large amounts of sulfur vacancies, ^{46,47} these vacancies are not observed in our lattice-resolved lateral force images shown in Figure 4a–c. This is because the atomic vacancies may be either below the surface and thus not detected by AFM, or present at low concentration at the surface and do not contribute to the lattice image of the lateral force signal in

DC mode AFM (which results from the stick-slip motion of the tip⁴⁹).

Based on all the results shown in Figure 4, we observe that, despite the PZC variations and differences in the experimental observables, the overall width of the first EDL exhibits consistent trends for all the imaged areas. As shown in the green shaded regions in Figure 4, the first EDL is always the narrowest at PZC, and widens as the potential becomes more positive or more negative. This is likely due to the larger separation between EMIM⁺ and TFSI⁻ in their ion pairs and the tilting of molecules in the outer sub-layer as the EDL becomes more strongly charged (Figures 3, S6, S8, and S12). Therefore, the first EDL width contains information on both the intermolecular pairing distance and molecular orientation. Hence, this width value can be used as an approximate experimental descriptor of the EDL structure.

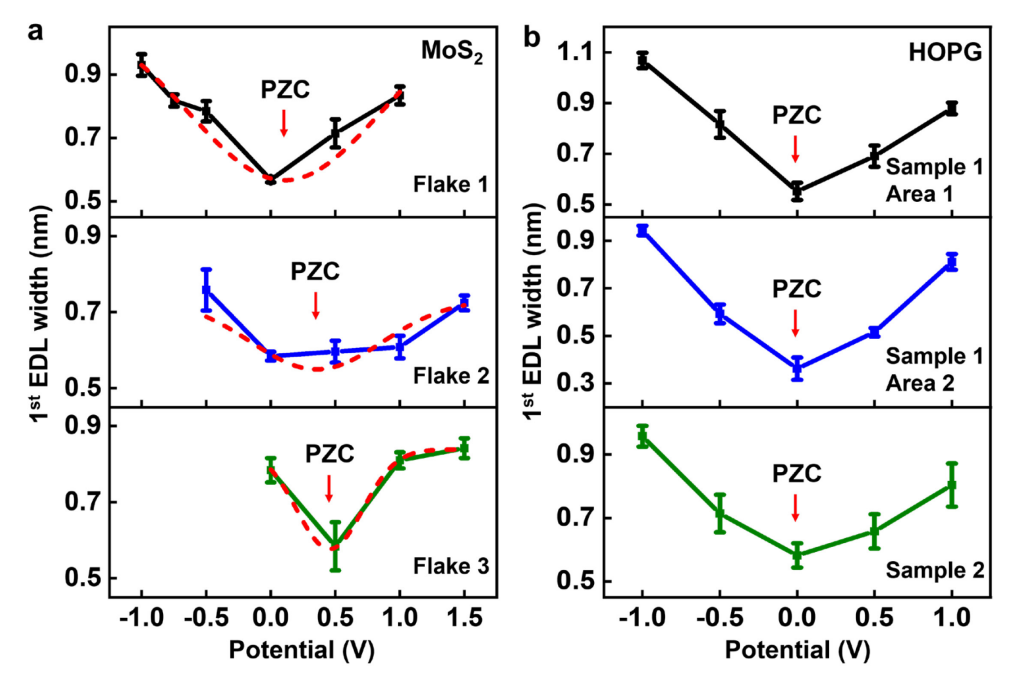


Figure 5. Summary of the 1st EDL width *vs* electrode potential (*vs* Pt) obtained from EC-3D-AFM. For each MoS₂ (**a**) and HOPG (**b**) system, multiple x-z frames at each potential are collected to obtain the average width of the 1st EDL as well as the standard deviation (shown as the error bars). The red dashed lines for the MoS₂ systems are guides to the eye to show the overall trend. In each plot, the potential corresponding to the estimated minimum width position is marked as PZC (0.11 V, 0.35 V, and 0.46 V for MoS₂, and ~0 V for HOPG).

We further analyze the 1st EDL width of multiple x-z frames at each potential for each local electrode region shown in Figure 4, and plot the average width and standard deviation in Figure 5. We observe that, for all the six electrode regions, the 1st EDL width *vs* potential plots show similar "V" shapes where the minimum position corresponds to the PZC. Consistent with results shown in Figure 4, MoS₂ flakes exhibit fluctuations in the PZC values, while HOPG always has PZC near 0 V (*vs* Pt). Therefore, this experimental descriptor of 1st EDL width reveals both the PZC and the capacitive charging process throughout different potentials.

In summary, through MD simulations and EC-3D-AFM experiments, we have identified the

innermost ion association configuration to be a key descriptor of the EDL structure and capacitive charging properties of EMIM-TFSI, a widely used, imidazolium-based ionic liquid. Experimentally, this descriptor is represented by the 1st EDL width. These theoretical and experimental descriptors are likely applicable to a large range of electrodes and highly ionic electrolytes, and will guide the rational design of electrode-electrolyte interfaces for applications in various electrochemical systems.

ASSOCIATED CONTENT

Supporting Information.

The Supporting Information is available free of charge at http://pubs.acs.org.

Methods: MD simulations, sample and tip preparation, cantilever calibration process, EC-3D-AFM measurements, EC-3D-AFM data analysis, confocal Raman measurements, KPFM.

Supporting Figures: Snapshot of the MoS₂/EMIM-TFSI/MoS₂ MD simulation system, Comparison of COM profiles averaged at different time periods of the MD production run, Snapshot of the HOPG/EMIM-TFSI/HOPG MD simulation system, MD simulated electrostatic profiles of EMIM-TFSI/MoS₂, Areal charge density in the first EDL as a function of the electrode's surface charge density of EMIM-TFSI/MoS₂, MD simulated molecular orientation of the EMIM-TFSI/MoS₂ system, MD simulated bulk angular distribution, MD simulation of the overall EDL molecular configuration of EMIM-TFSI/HOPG, Comparison of peak positions within the first EDL between MD and EC-3D-AFM results, Schematic of a possible real-time 3D-AFM imaging process, MD simulation of the intermolecular coordination structures of the 1st EDL of EMIM-TFSI on HOPG, Distribution of different types of EMIM⁺-TFSI⁻ ion pairs on HOPG, Comparison of AC mode phase *vs* z curves of EMIM-TFSI/HOPG and EMIM-TFSI/Si, Representative confocal Raman spectrum of MoS₂, Large-area AFM and confocal Raman maps of MoS₂ flakes, Large-area AFM and KPFM maps of MoS₂ flakes.

Supporting Tables specifying the AFM probe parameters and EC-3D-AFM imaging parameters.

Notes

The authors declare no competing financial interest.

ACKNOWLEDGMENT

Y.Z. and K.S.P. acknowledge the support from the Air Force Office of Scientific Research under award number FA9550-22-1-0014. Y.Z., F.Z. and S.Z. acknowledge the support from the Beckman Young Investigator Award provided by the Arnold and Mabel Beckman Foundation. H.W. and N.R.A. would like to acknowledge support from the National Science Foundation under Grant # 2140225.

REFERENCES

- (1) Ball, P. Water as an Active Constituent in Cell Biology. *Chem. Rev.* **2008**, *108*, 74–108.
- (2) Shannon, M. A.; Bohn, P. W.; Elimelech, M.; Georgiadis, J. G.; Mariñas, B. J.; Mayes, A. M. Science and Technology for Water Purification in the Coming Decades. *Nature* **2008**, 452, 301–310.
- (3) Stamenkovic, V. R.; Strmcnik, D.; Lopes, P. P.; Markovic, N. M. Energy and Fuels from Electrochemical Interfaces. *Nat. Mater.* **2017**, *16*, 57–69.
- (4) Hammes-Schiffer, S.; Galli, G. Integration of Theory and Experiment in the Modelling of Heterogeneous Electrocatalysis. *Nat. Energy* **2021**, *6*, 700–705.
- (5) Bard, A. J.; Faulkner, L. R. *Electrochemical Methods: Fundamentals and Applications*, 2nd ed.; Wiley: New York, 2001.
- (6) Velasco-Velez, J.-J.; Wu, C. H.; Pascal, T. A.; Wan, L. F.; Guo, J.; Prendergast, D.; Salmeron, M. The Structure of Interfacial Water on Gold Electrodes Studied by X-Ray Absorption Spectroscopy. *Science* **2014**, *346*, 831–834.
- (7) Li, C.-Y.; Le, J.-B.; Wang, Y.-H.; Chen, S.; Yang, Z.-L.; Li, J.-F.; Cheng, J.; Tian, Z.-Q. In Situ Probing Electrified Interfacial Water Structures at Atomically Flat Surfaces. *Nat. Mater.* **2019**, *18*, 697–701.
- (8) Montenegro, A.; Dutta, C.; Mammetkuliev, M.; Shi, H.; Hou, B.; Bhattacharyya, D.; Zhao, B.; Cronin, S. B.; Benderskii, A. V. Asymmetric Response of Interfacial Water to Applied Electric Fields. *Nature* **2021**, *594*, 62–65.
- (9) Favaro, M.; Jeong, B.; Ross, P. N.; Yano, J.; Hussain, Z.; Liu, Z.; Crumlin, E. J. Unravelling the Electrochemical Double Layer by Direct Probing of the Solid/Liquid Interface. *Nat. Commun.* **2016**, *7*, 12695.
- (10) Bohinc, K.; Kralj-Iglič, V.; Iglič, A. Thickness of Electrical Double Layer. Effect of Ion Size. *Electrochim. Acta* **2001**, *46*, 3033–3040.
- (11) Wang, Y.-H.; Zheng, S.; Yang, W.-M.; Zhou, R.-Y.; He, Q.-F.; Radjenovic, P.; Dong, J.-C.; Li, S.; Zheng, J.; Yang, Z.-L.; et al. In Situ Raman Spectroscopy Reveals the Structure and Dissociation of Interfacial Water. *Nature* **2021**, *600*, 81–85.
- (12) Shen, L.; Lu, B.; Li, Y.; Liu, J.; Huang-fu, Z.; Peng, H.; Ye, J.; Qu, X.; Zhang, J.; Li, G.; et al. Interfacial Structure of Water as a New Descriptor of the Hydrogen Evolution Reaction. *Angew. Chemie Int. Ed.* **2020**, *59*, 22397–22402.
- (13) Doblhoff-Dier, K.; Koper, M. T. M. Modeling the Gouy-Chapman Diffuse Capacitance with Attractive Ion-Surface Interaction. *J. Phys. Chem. C* **2021**, *125*, 16664–16673.
- (14) Daikhin, L. I.; Kornyshev, A. A.; Urbakh, M. Double-Layer Capacitance on a Rough Metal Surface. *Phys. Rev. E* **1996**, *53*, 6192–6199.
- (15) Rosen, B. A.; Salehi-Khojin, A.; Thorson, M. R.; Zhu, W.; Whipple, D. T.; Kenis, P. J. A.; Masel, R. I. Ionic Liquid–Mediated Selective Conversion of CO₂ to CO at Low Overpotentials. *Science* **2011**, *334*, 643–644.
- (16) Mohd Noor, S. A.; Howlett, P. C.; MacFarlane, D. R.; Forsyth, M. Properties of Sodium-

- Based Ionic Liquid Electrolytes for Sodium Secondary Battery Applications. *Electrochim. Acta* **2013**, *114*, 766–771.
- (17) Suo, L.; Borodin, O.; Gao, T.; Olguin, M.; Ho, J.; Fan, X.; Luo, C.; Wang, C.; Xu, K. "Water-in-Salt" Electrolyte Enables High-Voltage Aqueous Lithium-Ion Chemistries. *Science* **2015**, *350*, 938–943.
- (18) Wang, J.; Yamada, Y.; Sodeyama, K.; Watanabe, E.; Takada, K.; Tateyama, Y.; Yamada, A. Fire-Extinguishing Organic Electrolytes for Safe Batteries. *Nat. Energy* **2018**, *3*, 22–29.
- (19) Heckmann, A.; Thienenkamp, J.; Beltrop, K.; Winter, M.; Brunklaus, G.; Placke, T. Towards High-Performance Dual-Graphite Batteries Using Highly Concentrated Organic Electrolytes. *Electrochim. Acta* **2018**, *260*, 514–525.
- (20) Lukatskaya, M. R.; Feldblyum, J. I.; Mackanic, D. G.; Lissel, F.; Michels, D. L.; Cui, Y.; Bao, Z. Concentrated Mixed Cation Acetate "Water-in-Salt" Solutions as Green and Low-Cost High Voltage Electrolytes for Aqueous Batteries. *Energy Environ. Sci.* **2018**, *11*, 2876–2883.
- (21) Mao, X.; Brown, P.; Červinka, C.; Hazell, G.; Li, H.; Ren, Y.; Chen, D.; Atkin, R.; Eastoe, J.; Grillo, I.; et al. Self-Assembled Nanostructures in Ionic Liquids Facilitate Charge Storage at Electrified Interfaces. *Nat. Mater.* **2019**, *18*, 1350–1357.
- (22) Black, J. M.; Walters, D.; Labuda, A.; Feng, G.; Hillesheim, P. C.; Dai, S.; Cummings, P. T.; Kalinin, S. V; Proksch, R.; Balke, N. Bias-Dependent Molecular-Level Structure of Electrical Double Layer in Ionic Liquid on Graphite. *Nano Lett.* **2013**, *13*, 5954–5960.
- (23) Hayes, R.; Borisenko, N.; Tam, M. K.; Howlett, P. C.; Endres, F.; Atkin, R. Double Layer Structure of Ionic Liquids at the Au(111) Electrode Interface: An Atomic Force Microscopy Investigation. *J. Phys. Chem. C* **2011**, *115*, 6855–6863.
- (24) Segura, J. J.; Elbourne, A.; Wanless, E. J.; Warr, G. G.; Voïtchovsky, K.; Atkin, R. Adsorbed and near Surface Structure of Ionic Liquids at a Solid Interface. *Phys. Chem. Chem. Phys.* **2013**, *15*, 3320–3328.
- (25) Jurado, L. A.; Espinosa-Marzal, R. M. Insight into the Electrical Double Layer of an Ionic Liquid on Graphene. *Sci. Rep.* **2017**, *7*, 4225.
- (26) Sheehan, A.; Jurado, L. A.; Ramakrishna, S. N.; Arcifa, A.; Rossi, A.; Spencer, N. D.; Espinosa-Marzal, R. M. Layering of Ionic Liquids on Rough Surfaces. *Nanoscale* **2016**, *8*, 4094–4106.
- (27) Hayes, R.; El Abedin, S. Z.; Atkin, R. Pronounced Structure in Confined Aprotic Room-Temperature Ionic Liquids. *J. Phys. Chem. B* **2009**, *113*, 7049–7052.
- (28) Rakov, D. A.; Chen, F.; Ferdousi, S. A.; Li, H.; Pathirana, T.; Simonov, A. N.; Howlett, P. C.; Atkin, R.; Forsyth, M. Engineering High-Energy-Density Sodium Battery Anodes for Improved Cycling with Superconcentrated Ionic-Liquid Electrolytes. *Nat. Mater.* **2020**, *19*, 1096–1101.
- (29) Zhang, R.; Han, M.; Ta, K.; Madsen, K. E.; Chen, X.; Zhang, X.; Espinosa-Marzal, R. M.; Gewirth, A. A. Potential-Dependent Layering in the Electrochemical Double Layer of

- Water-in-Salt Electrolytes. ACS Appl. Energy Mater. 2020, 3, 8086–8094.
- (30) Bazant, M. Z.; Storey, B. D.; Kornyshev, A. A. Double Layer in Ionic Liquids: Overscreening versus Crowding. *Phys. Rev. Lett.* **2011**, *106*, 46102.
- (31) McEldrew, M.; Goodwin, Z. A. H.; Kornyshev, A. A.; Bazant, M. Z. Theory of the Double Layer in Water-in-Salt Electrolytes. *J. Phys. Chem. Lett.* **2018**, *9*, 5840–5846.
- (32) Benaglia, S.; Uhlig, M. R.; Hernández-Muñoz, J.; Chacón, E.; Tarazona, P.; Garcia, R. Tip Charge Dependence of Three-Dimensional AFM Mapping of Concentrated Ionic Solutions. *Phys. Rev. Lett.* **2021**, *127*, 196101.
- (33) Watanabe, M.; Thomas, M. L.; Zhang, S.; Ueno, K.; Yasuda, T.; Dokko, K. Application of Ionic Liquids to Energy Storage and Conversion Materials and Devices. *Chem. Rev.* **2017**, 117, 7190–7239.
- (34) Asadi, M.; Kumar, B.; Liu, C.; Phillips, P.; Yasaei, P.; Behranginia, A.; Zapol, P.; Klie, R. F.; Curtiss, L. A.; Salehi-Khojin, A. Cathode Based on Molybdenum Disulfide Nanoflakes for Lithium–Oxygen Batteries. *ACS Nano* **2016**, *10*, 2167–2175.
- (35) Asadi, M.; Kim, K.; Liu, C.; Addepalli, A. V.; Abbasi, P.; Yasaei, P.; Phillips, P.; Behranginia, A.; Cerrato, J. M.; Haasch, R.; et al. Nanostructured Transition Metal Dichalcogenide Electrocatalysts for CO₂ Reduction in Ionic Liquid. *Science* **2016**, *353*, 467–470.
- (36) Asadi, M.; Kumar, B.; Behranginia, A.; Rosen, B. A.; Baskin, A.; Repnin, N.; Pisasale, D.; Phillips, P.; Zhu, W.; Haasch, R.; et al. Robust Carbon Dioxide Reduction on Molybdenum Disulphide Edges. *Nat. Commun.* **2014**, *5*, 4470.
- (37) Wang, X.; Salari, M.; Jiang, D.; Chapman Varela, J.; Anasori, B.; Wesolowski, D. J.; Dai, S.; Grinstaff, M. W.; Gogotsi, Y. Electrode Material-Ionic Liquid Coupling for Electrochemical Energy Storage. *Nat. Rev. Mater.* 2020, 5, 787–808.
- (38) Vatamanu, J.; Hu, Z.; Bedrov, D.; Perez, C.; Gogotsi, Y. Increasing Energy Storage in Electrochemical Capacitors with Ionic Liquid Electrolytes and Nanostructured Carbon Electrodes. *J. Phys. Chem. Lett.* **2013**, *4*, 2829–2837.
- (39) Lin, M.-C.; Gong, M.; Lu, B.; Wu, Y.; Wang, D.-Y.; Guan, M.; Angell, M.; Chen, C.; Yang, J.; Hwang, B.-J.; et al. An Ultrafast Rechargeable Aluminium-Ion Battery. *Nature* **2015**, 520, 324–328.
- (40) Uhlig, M. R.; Martin-Jimenez, D.; Garcia, R. Atomic-Scale Mapping of Hydrophobic Layers on Graphene and Few-Layer MoS₂ and WSe₂ in Water. *Nat. Commun.* **2019**, *10*, 2606.
- (41) Zhou, S.; Panse, K. S.; Motevaselian, M. H.; Aluru, N. R.; Zhang, Y. Three-Dimensional Molecular Mapping of Ionic Liquids at Electrified Interfaces. ACS Nano 2020, 14, 17515– 17523.
- (42) Page, A. J.; Elbourne, A.; Stefanovic, R.; Addicoat, M. A.; Warr, G. G.; Voïtchovsky, K.; Atkin, R. 3-Dimensional Atomic Scale Structure of the Ionic Liquid–Graphite Interface Elucidated by AM-AFM and Quantum Chemical Simulations. *Nanoscale* **2014**, *6*, 8100–

8106.

- (43) Atkin, R.; Warr, G. G. Structure in Confined Room-Temperature Ionic Liquids. *J. Phys. Chem. C* **2007**, *111*, 5162–5168.
- (44) Wang, S.; Li, S.; Cao, Z.; Yan, T. Molecular Dynamic Simulations of Ionic Liquids at Graphite Surface. *J. Phys. Chem. C* **2010**, *114*, 990–995.
- (45) Haskins, J. B.; Lawson, J. W. Evaluation of Molecular Dynamics Simulation Methods for Ionic Liquid Electric Double Layers. *J. Chem. Phys.* **2016**, *144*, 184707.
- (46) Hong, J.; Hu, Z.; Probert, M.; Li, K.; Lv, D.; Yang, X.; Gu, L.; Mao, N.; Feng, Q.; Xie, L.; et al. Exploring Atomic Defects in Molybdenum Disulphide Monolayers. *Nat. Commun.* **2015**, *6*, 6293.
- (47) Vancsó, P.; Magda, G. Z.; Pető, J.; Noh, J.-Y.; Kim, Y.-S.; Hwang, C.; Biró, L. P.; Tapasztó, L. The Intrinsic Defect Structure of Exfoliated MoS₂ Single Layers Revealed by Scanning Tunneling Microscopy. *Sci. Rep.* **2016**, *6*, 29726.
- (48) Ziegler, D.; Stemmer, A. Force Gradient Sensitive Detection in Lift-Mode Kelvin Probe Force Microscopy. *Nanotechnology* **2011**, *22*, 75501.
- (49) Carpick, R. W.; Salmeron, M. Scratching the Surface: Fundamental Investigations of Tribology with Atomic Force Microscopy. *Chem. Rev.* **1997**, *97*, 1163–1194.